Aerospace Science and Technology 111 (2021) 106533

Contents lists available at ScienceDirect

Aerospace Science and Technology

www.elsevier.com/locate/aescte

Civil turbofan propulsion aerodynamics: Thrust-drag accounting and impact of engine installation position

Ioannis Goulos [a,*], John Otter [a], Fernando Tejero [a], Josep Hueso Rebassa [a], David MacManus [a], Christopher Sheaf [b]

[a] Propulsion Engineering Centre, School of Aerospace Transport and Manufacturing, Cranfield University, Bedfordshire, MK43 0AL, UK
[b] Installation Aerodynamics, Rolls-Royce plc, Trent Hall 2.2, Derby, DE24 8BJ, UK

ARTICLE INFO

Article history:
Received 1 June 2020
Received in revised form 9 December 2020
Accepted 21 January 2021
Available online 28 January 2021
Communicated by Dionysios Angelidis

Keywords:
Aerospace engineering
Turbofan
Aerodynamics
Computational fluid dynamics
Thrust and drag accounting
Class-shape transformation

ABSTRACT

It is envisaged that the next generation of civil aero-engines will employ high bypass ratios to lower specific thrust and improve propulsive efficiency. This trend is likely to be accompanied with the integration of compact nacelle and exhausts in podded under-wing installation positions that are close coupled to the airframe. This leads to the requirement for a comprehensive methodology able to predict aerodynamic performance for combined airframe-engine architectures. This paper presents a novel thrust and drag accounting approach for the aerodynamic analysis of integrated airframe-engine systems. An integral metric is synthesised based on the concept of net vehicle force. This is accomplished through the consolidation of aerodynamic coefficients, combined with the engine cycle characteristics obtained from a thermodynamic matching model. The developed approach is coupled with an in-house tool for the aerodynamic design and analysis of installed aero-engines. This framework is deployed to quantify the impact of engine installation position on the aerodynamic performance of a future large turbofan installed on a commercial wide-body airframe. The governing flow mechanisms are identified and their influence is decomposed in terms of the impact on airframe, nacelle, and exhaust performance. It is shown that it is essential to include the impact of installation on the exhaust for the correct determination of overall airframe-engine performance. The difference in net vehicle force for a close coupled position can reach up to -0.70% of nominal standard net thrust relative to a representative baseline engine location.

1. Introduction

1.1. Background

Current design trends for civil aero-engines dictate increasing By-Pass Ratio (BPR) to lower specific thrust and improve propulsive efficiency [1]. However, an increase in BPR for a given net thrust is typically accompanied by an increase in engine size, nacelle wetted-area, and fan diameter D_{fan} [2]. This increase in BPR results in higher exchange rates between nacelle and exhaust aerodynamic performance, and engine Specific Fuel Consumption (SFC) [3]. An increase in BPR from 11 to 15+ at fixed standard net thrust F_N, raises the gross to net thrust ratio from 3 to 4 [4]. Since gross thrust is dependent on the exhaust velocity coefficient C_v [5], this change in BPR can increase the exchange rate between exhaust performance and SFC by 33% relative to contemporary engines [6]. As regards the impact on the nacelle, an increase in D_{fan} can incur additional weight and drag penalties [7]. Daggett [8] noted that the replacement of a conventional turbofan ($BPR = 7$ and $D_{fan} = 3.175$ m) to a geared configuration ($BPR = 14.3$ and $D_{fan} = 3.861$ m) can increase nacelle drag by 30% on a four-engine aircraft. The geometry of a power-plant with separate-jets is shown in Fig. 1(a).

Future Very-High Bypass Ratio (VHBR) engines are expected to be more close coupled to the wing due to wing-flutter, pylon structural requirements, as well as ground clearance considerations associated with a larger D_{fan} [9]. As a result, the impact of installation due to the aerodynamic interaction between the airframe and the power-plant is expected to increase for future aero-engines compared to contemporary architectures [10,11]. Figs. 1(b) and (c) illustrate the geometry of an installed VHBR aero-engine within a podded under-wing installation position. The manifestation of adverse installation effects can influence the aerodynamic

* Corresponding author.
E-mail addresses: i.goulos@cranfield.ac.uk, i.goulos@gmail.com (I. Goulos).

https://doi.org/10.1016/j.ast.2021.106533

Nomenclature

Roman Symbols

$\dot{m}$ and $\dot{m}_f$	Mass flow and fuel flow rate, respectively ... kg/sec
$\vec{dS}$ and $\vec{dA}$	Surface normal and tangential unit vectors, respectively
$\vec{e}_D$, $\vec{e}_S$, $\vec{e}_L$	Aerodynamic axes reference frame unit vectors
$\vec{e}_X$, $\vec{e}_Y$, $\vec{e}_Z$	Airframe axes reference frame unit vectors
$\vec{e}_x$, $\vec{e}_y$, $\vec{e}_z$	Engine axes reference frame unit vectors
C_d and C_v	Exhaust nozzle discharge and velocity coefficient
C_L and C_D	Lift and drag coefficients
C_p^{mod}	Modified static pressure coefficient, $= \frac{p - p_\infty}{p_\infty}$
C_{ref} and A_{ref}	Reference chord length and area, respectively ..... m and m^2
D_{fan}	Fan diameter ..... m
dx and dz	Nacelle TE axial and vertical offset from wing LE position ..... m
F_G	Gauge stream force ..... N
F_N and $F_N^{Nom.}$	Standard net thrust and nominal standard net thrust rating ..... N
k	Turbulent kinetic energy ..... m^2/sec^2
$L_{A/F}$ and $D_{A/F}$	Airframe lift and drag ..... N
L^*_{nac} and D^*_{nac}	Modified nacelle lift and drag ..... N
M and Re	Mach and Reynolds number
p and T	Static pressure and temperature, respectively ..... Pa and K
P_0, T_0	Stagnation pressure and temperature, respectively ..... Pa and K
V and $\vec{V}$	Flow velocity and velocity vector, respectively m/sec
y^+	Non-dimensional wall distance

Greek Symbols

α_{eng} and $\alpha_{A/F}$	Engine and airframe effective incidence angle ..... deg
γ	Specific heat capacity ratio
κ	Thermal conductivity ..... J/(m×K×sec)
λ	Total to ambient static nozzle pressure ratio
ω	Specific dissipation rate 1/sec
ρ	Flow density ..... kg/m^3
τ	Viscous shear stress ..... Pa
θ and ϕ	Force exerted by fluid in thrust and drag domains . N
θ_{pitch} and θ_{toe}	Engine installation pitch and toe angles .... deg

Superscripts

$*$	Modified metric definition - inclusion of after-body terms
A/C	Referring to the whole aircraft
A/F	Referring to the airframe only (wing, fuselage, and tailplane)
$Bypass$	Referring to the bypass nozzle
$Core$	Referring to the core nozzle
$Cycle$	Quantity obtained from engine cycle characteristics
$Ideal$	Referring to isentropically fully-expanded flow conditions
$Vent$	Referring to the vent nozzle

Subscripts

$0-5$	Referring to the denoted engine station number
∞, is	Referring to free-stream and isentropic conditions, respectively
D,S,L	Component resolved in the aerodynamic axes system
hi	Referring to intake highlight plane
X,Y,Z	Component resolved in the airframe axes system
x,y,z	Component resolved in the engine axes system

Acronyms

$CNPR$	Core Nozzle Pressure Ratio, $= \frac{P_{05}}{p_\infty}$
$FNPR$	Fan Nozzle Pressure Ratio, $= \frac{P_{03}}{p_\infty}$
GPF	Gross Propulsive Force ..... N
$MFCR$	Mass Flow Capture Ratio, $= \frac{A_\infty}{A_{hi}}$
NPF	Net Propulsive Force ..... N
NVF	Net Vehicle Force ..... N
$VNPR$	Vent Nozzle Pressure Ratio, $= \frac{P_{04}}{p_\infty}$

behaviour of the airframe, nacelle, and the exhaust [12] (Fig. 1(c)). Sibili et al. [13] reported that engine integration within a highly close coupled position can result in a cruise SFC increase of approximately 2.5% compared to a contemporary engine placement. Thus, adverse installation effects that can arise for close coupled installation positions can potentially outweigh the beneficial impact on propulsive efficiency gained from VHBR cycles [14].

The increased sensitivity of SFC to nacelle and exhaust performance, combined with close coupled installation positions, lead to the requirement for a holistic method for the evaluation of integrated engine-airframe architectures. To achieve the fuel burn improvements of VHBR cycles [1,3], it is imperative that the trade-off between overall aerodynamic performance and installation position is understood. Furthermore, it is essential that the impact of engine position on the aerodynamic characteristics is decomposed to its constituent elements of airframe, nacelle, and exhaust performance changes. This can enable informed decisions in balancing aerodynamic [12] and non-aerodynamic considerations [9].

The impact of installation on the exhaust is particularly important for VHBR aero-engines due to the high exchange rate between exhaust C_v and SFC [4]. This aspect has not been previously investigated systematically for close coupled engine installation positions [15]. Consequently, there is a need to understand and quantify the impact of the airframe on the exhaust, as well as to account for this effect in the analysis of close coupled integrated airframe-engine systems. This process entails a thrust and drag accounting formulation [16] that determines the aerodynamic performance for combined airframe-engine systems, and decomposes the installation penalty to its constituent elements [17,18].

1.2. Thrust and drag accounting for installed aero-engines

The impact of civil aero-engine installation for podded underwing configurations has been traditionally investigated both computationally and experimentally [9]. Accurate prediction of exhaust performance plays a key role in the determination of in-flight installed thrust and drag [16]. Although research has been carried out in the field of in-flight thrust measurement [19], this is not currently considered to be a practical option [18]. As a result, in-flight thrust is usually deduced indirectly based on the engine operating point, whilst aircraft drag is determined based on the thrust requirement for trimmed flight [17,18,20]. Specifically, in-flight gross thrust is estimated based on the ideal thrust determined through the measured bypass and core nozzle inlet total pressures (Fig. 1(a)), corrected with an exhaust velocity coefficient C_v that is evaluated based on static ground tests [20]. However, the

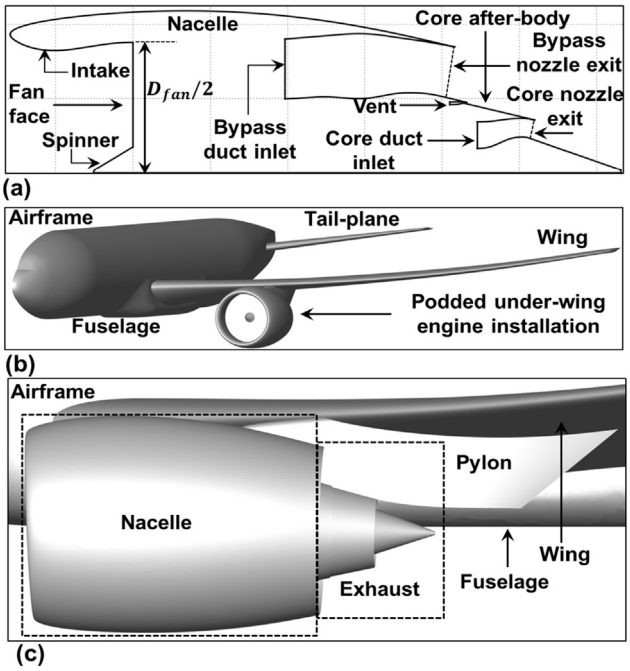

Fig. 1. Installed VHBR engine geometry: (a) Intake, nacelle, and separate-jet exhaust components, (b) podded under-wing installation, and (c) close coupled installation position.

validity of this approach can be compromised if the aerodynamic behaviour of the exhaust varies between static calibration tests and in-flight conditions [21]. Thus, accurate prediction of in-flight thrust and drag requires knowledge of the impact of installation on the exhaust, as well as accurate estimates of the engine cycle parameters.

The use of Reynolds Averaged Navier-Stokes (RANS) Computational Fluid Dynamics (CFD) has been established as a useful tool for the prediction of installed thrust and drag of civil aero-engines [22,23]. Modern CFD-based thrust and drag extraction methods can be classified under two categories: (a) far-field [24–27] and (b) near-field methods [12,22,23,28–30]. Several investigations have been reported where near-field and far-field methods have been compared in terms of their ability to predict airframe drag. A difference of 10-20 airframe drag counts has been found between the two methods [24,26].

Yufei et al. [22] applied a near-field approach based on RANS CFD for the prediction of installed powered-nacelle aerodynamic performance. A Thrust-Drag Bookkeeping (TDB) method based on control volume theory was employed to estimate the nacelle and exhaust aerodynamic coefficients. The impact of aero-engine installation was evaluated at mid-cruise conditions using bespoke nacelle and pylon designs coupled to a generic twin-jet civil airframe geometry. The method was applied to estimate the impact of jet momentum and enthalpy efflux on the wing static pressure distributions and aircraft drag polar. The work of Yufei et al. [22] highlighted the importance of accurately predicting exhaust C_v for powered-on conditions. However, the TDB method was based on a linear extrapolation of exhaust C_v from static testing ($M_\infty \approx 0$) to cruise conditions ($M_\infty \approx 0.785$) in order to account for the effect of free-stream Mach number M_∞. Thus, this approach proposed by Yufei et al. [22] does not capture the impact of the installed pressure field on the aerodynamic behaviour of the nacelle and the exhaust.

Stankowski et al. [12,30] and Otter et al. [15] investigated the impact of engine architecture and installation position on the aerodynamic behaviour of a wide-body 300-seater aircraft using RANS CFD. A parametric geometry definition based on intuitive Class-Shape Transformation functions (iCSTs) [31] was employed for the design of the nacelle [32,33], intake [34,35], and exhaust [36,37]. Analyses were carried out for two engines with a BPR of 11 and 18, respectively, installed on the NASA Common Research Model (CRM) [38]. The study assessed the impact of engine installation position on interference drag [12,30], as well as exhaust velocity and discharge coefficients, C_v and C_d, respectively [15]. However, the work of Stankowski et al. [12,30] and Otter et al. [15] did not include close coupled positions which could be considered for VHBR configurations [9]. Furthermore, the impact of the pylon was neglected.

1.3. Rationale

The numerical methods for the determination of installed thrust and drag outlined above, are based on predictions of jet momentum and enthalpy efflux derived from CFD simulations. These analyses are carried out with prescribed values of total pressure P_0 and temperature T_0 at the bypass and core nozzle inlet boundaries (Fig. 1(a)). However, for fixed values of P_0 and T_0 at each nozzle inlet, the effect of external flow suppression can alter the bypass and core nozzle mass, momentum, and enthalpy fluxes [21]. Furthermore, the back-pressure at the fan Outlet Guide Vane (OGV) and Low-Pressure Turbine (LPT) OGV can also be affected accordingly [21]. This can influence the operating point of the engine and force it to operate at Off-Design (OD) conditions with a concurrent impact on P_0 and T_0 at the bypass and core nozzle inlet [39].

To account for the impact of the installed flow-field on the bypass and core nozzle exit conditions, the manufacturer may re-size the nozzle throat areas to achieve the required mass, momentum, and enthalpy efflux [15]. This establishes compatibility of the installed exhaust system with the engine cycle at Design Point (DP) and mitigates any sub-optimal OD operation. However, this may not be a practical option within a design optimisation environment where multiple analyses need to be carried out for a range of installation positions.

From a thrust and drag accounting viewpoint, changes to the computed jet momentum and enthalpy efflux due to the installed flow-field, may lead to variations in the bypass and core nozzle exit mass flows and stream forces. As a result, for numerical analyses with fixed bypass and core inlet P_0 and T_0, as well as fixed nozzle throat areas, this classical CFD-based TDB approach [12,22,23,28–30] may result in misleading estimates of installed engine thrust.

Therefore, the impact of installed external flow suppression [21] on the compatibility between exhaust jet momentum and enthalpy efflux, and the prescribed engine cycle characteristics has been ignored within previously derived near-field [12,22,23,28–30] as well as far-field [24–27] formulations. This modelling deficiency can potentially upset the balance between the installed thrust and drag terms [15]. This could lead to erroneous trends within a design space exploration environment where the focus is placed on overall aircraft performance, rather than on individual system components (Fig. 1(a)).

1.4. Scope of present work

This paper presents a novel thrust and drag accounting approach based on CFD, for the aerodynamic analysis of installed aero-engines. The proposed approach integrates key elements of TDB methods employed in computational analyses [12,22,23,28–30] and in-flight testing [18,20]. This is achieved by combining the airframe, nacelle, and exhaust aerodynamic coefficients obtained from CFD with the prescribed engine cycle characteristics [39]. The developed TDB methodology attempts to establish compatibility between exhaust jet momentum and enthalpy efflux, and

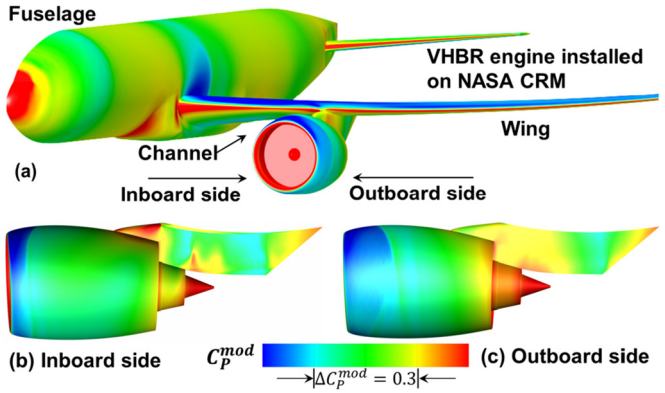

Fig. 2. Example computation example for a VHBR engine installed on the NASA CRM - variation of $C_p^{mod} = \frac{p - p_\infty}{p_\infty}$: (a) whole aircraft, (b) engine inboard, and (c) engine outboard. (For interpretation of the colours in the figure(s), the reader is referred to the web version of this article.)

the prescribed engine operating point. An analytical formulation is employed for the parametric design of installed aero-engine nacelles [32,33], intakes [34,35], exhausts [36,37] and pylons [40] based on iCST functions [31]. The NASA CRM [38] is utilised for the representation of a typical wide-body commercial transport airframe geometry. This installed aero-engine design approach is coupled with an automatic hybrid mesh generator [41], as well as a viscous and compressible flow solver [42].

This devised novel TDB approach is employed to quantify the aerodynamic penalty associated with close coupled installation positions for a future VHBR aero-engine. Comparative evaluations are carried out for conventional and close coupled positions. The overall installation penalty is decomposed to its constituent elements in terms of impact on airframe, nacelle, and exhaust performance, whilst the governing flow mechanisms are identified and exposed.

2. Methodology

A numerical framework is developed in this article for the aerodynamic analysis of installed turbofan engines with separate-jet exhausts. This proposed method extends previous work done by Goulos et al. [4,6,36,37,43] on the aerodynamic design and analysis of civil aero-engines, to the performance evaluation of integrated airframe-engine architectures. This framework can automatically design, mesh, and simulate the geometry of an installed turbofan engine based on designated airframe and power-plant specifications. The system encompasses modelling methods developed for; engine performance simulation [44], parametric geometry definition of engine housing components [32–36,6], and RANS CFD flow solution [41,42]. An example computation of the normalised static pressure distribution $C_p^{mod} = \frac{p - p_\infty}{p_\infty}$ on the aircraft surfaces for a VHBR engine installed on the NASA CRM [38] is shown in Fig. 2.

2.1. Engine performance simulation and cycle analysis

The analysis commences by analysing the aero-thermal behaviour of the power-plant. Simulation is carried out using the method TURBOMATCH [44]. TURBOMATCH has been previously deployed and validated in several studies available in the existing literature for the prediction of DP, OD, transient, and degraded performance of gas-turbine engines [45–47]. TURBOMATCH is based on zero-dimensional (0D) aero-thermodynamic analysis of gas turbine engines using discrete component maps. The method also accounts for the impact of on-board electric and electronic systems' power off-takes. The method solves for the mass and energy balance between the various engine components. A non-linear and globally convergent "matrix-iteration" scheme is used to satisfy the required matching constraints in terms of turbine and nozzle non-dimensional flow capacities [39]. The goal of this process is three-fold: (a) it establishes the throat-area demand for the bypass and core nozzles, (b) it determines the averaged stagnation pressure P_0 and temperature T_0 at the inlet of each nozzle, as well as the engine inlet mass flow $\dot{m}_0$ (Fig. 1(a)) to be used as Boundary Conditions (BCs) in the CFD analysis, and (c) it establishes the ideal isentropic exhaust mass, momentum, and enthalpy effluxes that are compatible with the engine cycle. The system also models the air-flow vent that is usually located on the core after-body and is used to exhaust secondary air-flows (Fig. 1(a)) [6].

2.2. Thrust and drag accounting methodology

Fig. 3 illustrates the thrust and drag accounting reference system including the engine station numbering and nomenclature used in this work [17,18]. The unit vectors $\vec{e}_x$, $\vec{e}_y$, and $\vec{e}_z$ (Fig. 3(a)) denote the engine axes reference system, with $\vec{e}_x$ aligned with the engine centre line. The engine centre line is rotated relative to airframe reference axes system through application of the engine orientation pitch and toe angles, θ_{pitch} and θ_{toe}, respectively (Fig. 4). The airframe axes system is aligned with the fuselage centre line and is annotated by vectors $\vec{e}_X$, $\vec{e}_Y$, and $\vec{e}_Z$ (Fig. 4). An aerodynamic reference frame is defined to account for aircraft incidence effects. This frame is represented by the unit vectors $\vec{e}_D$, $\vec{e}_S$, and $\vec{e}_L$ (Fig. 3(a)), with $\vec{e}_D$ defined to be parallel with the undisturbed free-stream flow. The aerodynamic axes reference frame is rotated relative to the engine axes system through the effective engine incidence angle α_{eng} (Fig. 3(a)). Within this work, all aerodynamic forces are resolved in the aerodynamic axes frame of reference ($\vec{e}_D$, $\vec{e}_S$, and $\vec{e}_L$) [17,18].

The symbols θ and ϕ in Fig. 3(b) represent the aerodynamic forces exerted by the fluid flow on the wall surfaces and streamtube boundaries, within the thrust and drag domains, respectively. All wall forces, θ and ϕ, are evaluated through numerical integration of gauge static pressure and shear-stress terms along the viscous surfaces. A dividing streamline is identified on the pylon based on surface T_0 distribution to differentiate between forces exerted in the thrust and drag domains, θ_{pylon} and ϕ_{pylon}, respectively. Numerical integration is used to calculate the gauge stream forces F_G [21] and mass flow rates $\dot{m}$ at the fan face (2), bypass (3), vent (4), and core (4) inlet boundaries (Fig. 3)(b). Within the following analysis, the subscripts L and D signify that the annotated forces have been resolved in the aerodynamic lift and drag axes, respectively, which are designated by unit vectors $\vec{e}_L$ and $\vec{e}_D$ (Fig. 3(a)). With these provisions, the wall forces θ and ϕ, and gauge stream forces F_G can be expressed as follows [15]:

$$(\phi, \theta)_D = \iint_{surface} (p - p_\infty)\vec{e}_D \cdot d\vec{S} + \iint_{surface} \tau \vec{e}_D \cdot d\vec{A} \tag{1}$$

$$(F_G)_D = \iint_{Area} (\rho |\vec{V}| \vec{V} \cdot \vec{e}_x + (p - p_\infty)) d\vec{S} \cdot \vec{e}_D \tag{2}$$

where p and τ are the local static pressure and viscous shear stress, respectively, whilst $\vec{V}$ denotes the local velocity vector expressed in the engine axes system (Fig. 3(a)). The symbols $d\vec{S}$ and $d\vec{A}$ signify the local surface normal and tangential unit vectors, respectively.

The exhaust aerodynamic performance is quantified using the modified velocity coefficient $(C_v^*)_D$ [15]. This coefficient represents the ratio of computed modified gross propulsive force $(GPF^*)_D$,

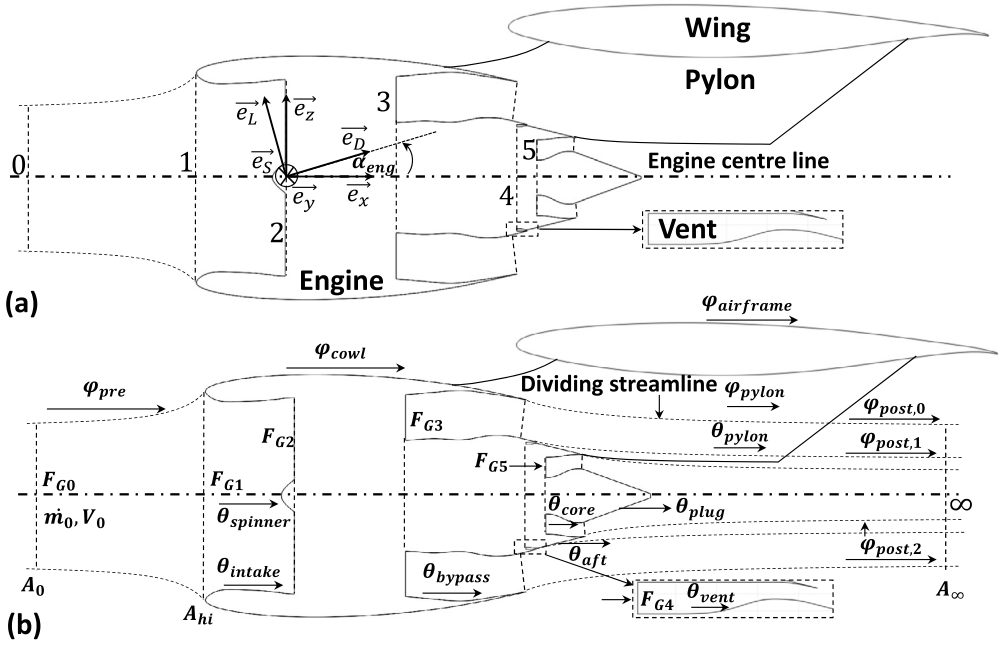

Fig. 3. Thrust and drag accounting system for installed turbofans with separate-jet exhausts: (a) Reference coordinate systems and engine station numbering, and (b) distribution of gauge stream, wall, and streamline aerodynamic forces.

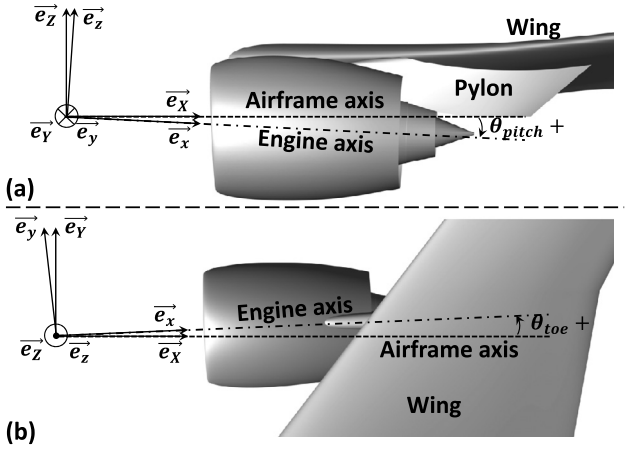

Fig. 4. Definition of engine orientation angles relative to airframe axes: (a) pitch angle θ_{pitch} and (b) toe angle θ_{toe}.

normalised with the calculated isentropic fully-expanded exhaust momentum efflux. The definition of $(C_v^*)_D$ is:

$$(C_v^*)_D = \frac{(GPF^*)_D}{\dot{m}_3 V_3^{Ideal} + \dot{m}_4 V_4^{Ideal} + \dot{m}_5 V_5^{Ideal}} \tag{3}$$

The modified gross propulsive force $(GPF^*)_D$ represents the aerodynamic force component in the free-stream flow direction, $\vec{e}_D$, that is produced solely by the exhaust system [15]. The superscript $()^*$ in the definition of $(C_v^*)_D$ denotes that the pressure and viscous forces exerted on the core after-body and plug (Fig. 3(b)) are included in the definition $(GPF^*)_D$ used in Eq. (3). Therefore, $(GPF^*)_D$ is adversely influenced by non-isentropic flow phenomena that manifest in the exhaust jet. These include boundary layer growth and skin friction within ducts, nozzles, and after-bodies (Fig. 1(a)), as well as viscous shear layers, shock waves, and expansion fans in the exhaust jet. The part of the pylon surface that is wetted by the exhaust jet is also accounted for within the definition $(GPF^*)_D$ (Eq. (4)). This is because the associated pressure and viscous forces reside within the "thrust domain" that is enclosed by the exhaust stream-tube boundary [18] (Fig. 3(b)). Based on the nomenclature of Figs. 3(a) and (b), the definition of $(GPF^*)_D$ is:

$$(GPF^*)_D = (F_{G3} + F_{G4} + F_{G5})_D - (\theta_{bypass} + \theta_{core} + \theta_{vent} + \theta_{aft} + \theta_{plug} + \theta_{pylon})_D \tag{4}$$

The term V^{Ideal} in the Right Hand Side (RHS) of Eq. (3) denotes the ideal jet velocity that corresponds to isentropic flow expansion to ambient static pressure p_∞, for each exhaust stream shown in Fig. 3(b). The associated definition is [36]:

$$V^{Ideal} = \sqrt{\frac{2\gamma RT_0}{(\gamma - 1)}\left(1 - \left(\frac{1}{\lambda}\right)^{\frac{\gamma - 1}{\gamma}}\right)} \tag{5}$$

where λ is the total to ambient static nozzle pressure ratio $\lambda = \frac{P_0}{p_\infty}$ for each exhaust stream (Fig. 3(b)), where P_0 and T_0 are prescribed at each duct inlet. The discharge coefficients for the bypass, vent, and core nozzles, C_d^{Bypass}, C_d^{Vent}, and C_d^{Core}, respectively (Fig. 1), are calculated based on the mass flow integrals at the corresponding inlet boundaries [36].

This definition for $(C_v^*)_D$ (Eq. (3)) results in a coefficient that is independent of exhaust mass efflux changes due to external flow suppression effects [21], that can adversely influence the calculation of installed gross propulsive force [15]. Furthermore, since $(C_v^*)_D$ is evaluated directly from CFD solutions for installed aero-engines, it includes the impact of installation effects that can alter the performance of the exhaust relative to an isolated engine. This effect was not accounted for in previous near-field TDB methods for the analysis of installed aero-engines [22]. Thus, for a given engine operating point, $(C_v^*)_D$ can be used to scale the ideal exhaust momentum efflux that is computed based on the engine cycle, to estimate the modified gross propulsive force $(GPF^*)_D^{Cycle}$ for an installed configuration. This process can be expressed as follows:

$$(GPF^*)_D^{Cycle} = (C_v^*)_D(\dot{m}_3{}^{Cycle}V_3^{Ideal} + \dot{m}_4{}^{Cycle}V_4^{Ideal} + \dot{m}_5{}^{Cycle}V_5^{Ideal}) \quad (6)$$

where the superscript $()^{Cycle}$ denotes that the exhaust mass flows used in the calculation of ideal exhaust momentum efflux in the RHS of Eq. (6), are estimated based on the corresponding engine cycle parameters [44]. This approach constitutes an adaptation of an established in-flight exhaust thrust measurement method [18,20] to a numerical TDB formulation. The objective is to establish compatibility between the computed exhaust momentum efflux and the engine operating point for the analysis of installed turbofan architectures.

The modified near-field drag extraction method [48] is employed for the computation of installed modified nacelle drag D_{nac}^*. The method is based on the estimation of the intake pre-entry force $(\phi_{pre})_D$ and fan cowl aerodynamic force $(\phi_{cowl})_D$ (Fig. 3). The nacelle geometry components required for the computation of D_{nac}^* include the fan cowl, spinner, and intake (Fig. 3). A 3D nacelle geometry was used in this work, as described by Tejero et al. [32,33]. For the purposes of installed engine analysis, the present method is extended with the inclusion of the aerodynamic force exerted on the part of the pylon surface that is not wetted by the exhaust jet $(\phi_{pylon})_D$ (Fig. 3). With these provisions, the installed modified nacelle drag D_{nac}^* can be expressed as follows:

$$D_{nac}^* = (\phi_{pre} + \phi_{cowl} + \phi_{pylon})_D \quad (7)$$

where the intake pre-entry force $(\phi_{pre})_D$, is calculated according to the modified near-field drag extraction method [48], as described below:

$$(\phi_{pre})_D = (F_{G2})_D - \dot{m}_0 V_0 - (\theta_{intk} + \theta_{spinner})_D \quad (8)$$

In this formulation [48], the impact of the exhaust jet on D_{nac}^* is accounted for through the modified static pressure field exerted on the nacelle after-body which serves to influence $(\phi_{cowl})_D$ (Eq. (7)). The aerodynamic forces due to the exhaust jet and free-stream flow exerted on the post-exit stream-tube boundary $(\phi_{post,0})_D$ (Fig. 3), are omitted both in the modified drag (D_{nac}^*) as well as the modified thrust domains $((GPF^*)_D^{Cycle})$. This is in accordance with the adapted thrust and drag accounting system [17,18]. However, it has been shown that the term $(\phi_{post,0})_D$ effectively cancels out in the definition of installed net propulsive force $(NPF)_D^{Cycle}$ (Eq. (9)), when D_{nac}^* and $(GPF^*)_D^{Cycle}$ are combined [17,18]. Therefore, the computation of $(NPF)_D^{Cycle}$ is not affected by this simplification.

Having established expressions for the installed modified gross propulsive force $(GPF^*)_D^{Cycle}$ and modified nacelle drag D_{nac}^*, the installed net propulsive force $(NPF)_D^{Cycle}$ can be computed, as follows:

$$(NPF)_D^{Cycle} = (GPF^*)_D^{Cycle} - \dot{m}_0 V_0 - D_{nac}^* \quad (9)$$

where $\dot{m}_0 V_0$ in the RHS of Eqs. (7) and (9) is the inlet momentum drag term. Having obtained an expression for $(NPF)_D^{Cycle}$, the method can be extended to the whole aircraft through inclusion of the airframe forces (Fig. 3(b)). These include the fuselage, wing, and tailplane (Fig. 2). The Net Vehicle Force (NVF) components can be resolved in the lift and drag axes, $\vec{e}_L$ and $\vec{e}_D$, respectively:

$$(NVF)_L = L_{A/F} + L_{nac}^* + (GPF^*)_L^{Cycle} \quad (10a)$$

$$(NVF)_D = D_{A/F} - (NPF)_D^{Cycle} \quad (10b)$$

where $L_{A/F} = (\phi_{airframe})_L$ and $D_{A/F} = (\phi_{airframe})_D$ are the airframe lift and drag, respectively. The terms L_{nac}^* and $(GPF^*)_L^{Cycle}$ in the RHS of Eq. (10a) represent the modified nacelle lift and gross propulsive force lift contribution, respectively. These are calculated using an approach that is identical to that applied in Eq. (7), where the aerodynamic forces are resolved in the lift $\vec{e}_L$ instead of the drag axis $\vec{e}_D$ (Fig. 3). Equations (10a) and (10b) can be employed to calculate the aircraft trim state in terms lift and propulsion, respectively.

Within this work, the aircraft is assumed to operate at mid-cruise conditions with $C_L^{A/C} = \frac{(NVF)_L}{0.5\rho_\infty V_\infty^2 A_{ref}} = 0.5$, where A_{ref} is the CRM reference area [38]. This condition effectively closes Eq. (10a), and it is satisfied by running a localised aircraft incidence sweep and by applying linear interpolation to match the desired $C_L^{A/C}$ [15]. Propulsive trim can be satisfied through enforcing the balance of installed thrust and drag by setting $(NVF)_D = 0$ in Eq. (10b) and by solving for the engine throttle setting which balances the installed net propulsive force with the airframe drag. This propulsive trim approach yields the engine fuel flow rate $\dot{m}_f$ as a figure of merit for overall aircraft performance. However, this process is computationally expensive and requires an iterative scheme to be applied around the engine performance model [44] and the CFD solver [42].

In order to mitigate the computational overhead associated with multiple CFD evaluations, this work adapts an integral metric based on the Left Hand Side (LHS) residual of Eq. (10b). This can be written as follows:

$$NVF = -(NVF)_D = (NPF)_D^{Cycle} - D_{A/F} \quad (11)$$

where the polarity in the definition of NVF (Eq. (11)) is reversed relative to Eq. (10b) so that a positive NVF delta indicates a benefit in overall aircraft performance. For relatively small changes in the engine operating point, the metrics of $\dot{m}_f$ and NVF are analogous. Otter [40] showed that, for a VHBR engine operating at mid-cruise conditions, and for changes in $\Delta(NVF)(\%)$ within a range of $(-15\%, +5\%)$ of F_N, $\dot{m}_f$ and NVF are proportional. This range in $\Delta(NVF)(\%)$ is substantially larger compared to expected changes in throttle setting for a given engine operating point due to adjustments of installation position [12,15], exhaust [4,6], or nacelle [32] design specifications.

2.3. Parametric geometry definition of civil aero-engines

The system incorporates the previously-developed parametric geometry definition based on iCST functions [31] for the design of the nacelle [32,33], intake [34,35], exhaust [6,36], and pylon [40], (Figs. 1(a) and (c)). The adapted iCST formulation defines the intake, nacelle, bypass/core duct and nozzle, and after-body annuli as functions of intuitive design parameters. The developed mathematical methods have been previously described extensively by Goulos et al. [4,6,36], Christie et al. [34,35], and Tejero et al. [32,33]. A parametric representation of the engine pylon is incorporated [40] (Figs. 2(b) and (c)). The pylon design is based on vertical stacking of planar iCST aerofoil sections and allows the automatic adjustment of the pylon geometry in an aerodynamically favourable manner for the engine installation position (Fig. 1(c)). This pylon design method has been shown to be highly-flexible and caters for a wide range of engine installation positions [40]. This parametric geometry definition has been previously deployed for the Design Space Exploration (DSE) of non-symmetric VHBR nacelle and exhaust architectures [40].

2.4. CFD methods and approach

The system employs a hemispherical domain (Fig. 5), which incorporates a half-model of the NASA CRM [38] (Fig. 2). The do-

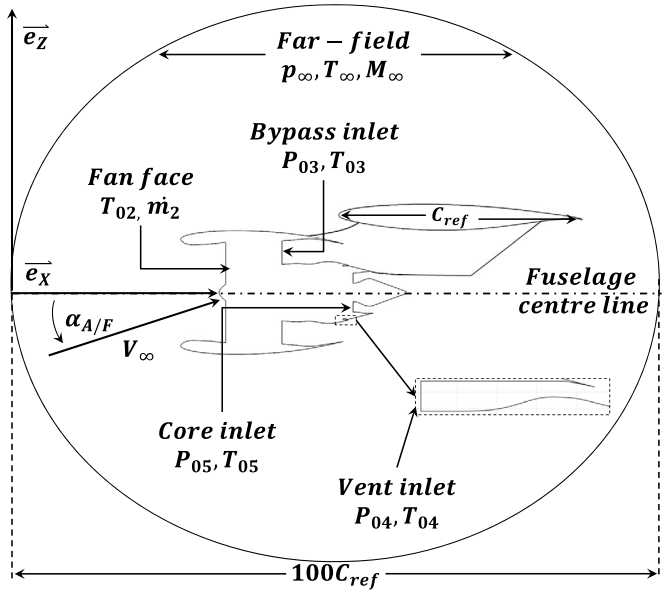

Fig. 5. Computational domain and boundary conditions.

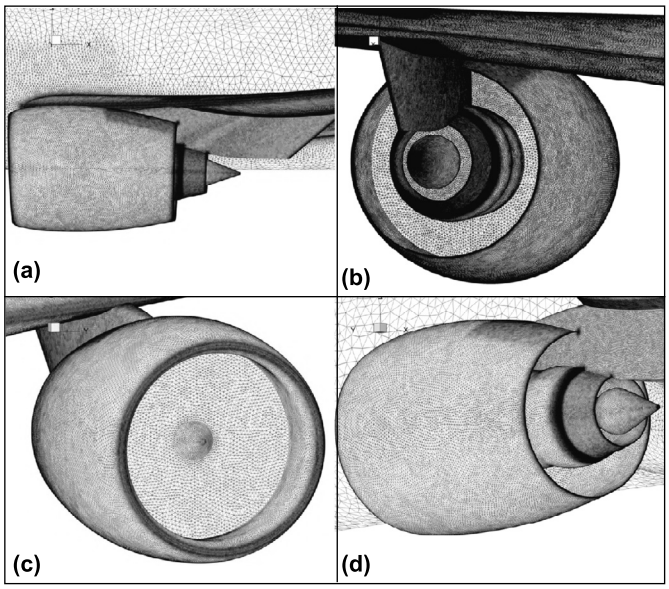

Fig. 6. Surface mesh close-up on engine and pylon surfaces: (a) engine outboard side, (b) exhaust and pylon after-body, (c) intake and spinner, and (d) nacelle and exhaust after-body.

main diameter is equal to $100 \times C_{ref}$, where C_{ref} is the CRM wing reference chord length [38]. This is in accordance with recommendations established through the 4^{th} AIAA drag prediction workshop [49]. The free-stream flow conditions are modelled using a pressure far-field BC with prescribed p_∞, M_∞, T_∞, applied at the hemispherical domain boundary. The airframe angle of attack $\alpha_{A/F}$ is defined by the free-stream flow direction relative to the vectors $\vec{e}_X$ and $\vec{e}_Z$. The engine fan face boundary is modelled as a pressure outlet with prescribed mass flow $\dot{m}_2$. The bypass, core, and vent inlet boundaries are modelled as pressure inlet BCs with defined P_0 and T_0. All thermodynamic parameters at the engine inlet and outlet boundaries are defined according to the cycle specifications [44]. All airframe, engine, and pylon surfaces are modelled as adiabatic and viscous no-slip walls.

A hybrid meshing methodology is employed [41]. Fig. 6 presents a close-up of the derived surface mesh on the engine and pylon surfaces. The developed approach employs structured prism layers near the viscous walls with $y^+ < 1$ for all wall-adjacent nodes. Tetrahedral elements are employed to populate the remainder of the computational domain in an unstructured manner. Near-wall unstructured mesh refinement is carried out based on local wall-curvature and surface-proximity features [41]. Unstructured mesh refinement zones are designated near the vicinity of the airframe, nacelle, and exhaust to resolve localised flow features. The employed spatial discretisation guidelines were established based on the grid verification and validation activities (section 2.5).

A grid independence analysis was carried out using meshes comprising 70×10^6, 130×10^6, and 288×10^6 elements. The second-order Grid Convergence Indices (GCI) [50] for $(NPF)_D^{Cycle}$ and $D_{A/F}$ corresponding to the medium mesh were found to be of the order of 0.36% and 0.024%, respectively. Consequently, meshes with approximately 130×10^6 elements were used for this study. The hybrid meshing approach [41] allows for automated mesh manipulation to account for changes to the engine installation position, as well as to the nacelle, exhaust, and pylon geometries.

Computations used an implicit, density-based, and compressible Favre averaged CFD approach [42] coupled with the $k-\omega$ Shear-Stress Transport (SST) turbulence model [51]. The Green-Gauss node based method was used for calculation of the flow-field gradients. A second-order accurate upwind scheme was used for the spatial discretisation of primitive variables, as well as turbulent kinetic energy k and specific dissipation rate ω. Thermal conductivity (κ) was computed according to kinetic theory [42]. Variable gas properties were employed using an 8^{th} order piecewise polynomial expression for the calculation of specific heat capacity as a function of static temperature [39]. Dynamic viscosity was calculated using Sutherland's law [52].

2.5. CFD method verification and validation

The CFD approach was validated in terms of airframe and installation drag using experimental data for the NASA CRM [53]. A grid sensitivity analysis was carried out to quantify the impact of CFD numerical uncertainty on the prediction of airframe drag. The domain and grid generation process was developed in accordance with the recommendations established through the 4^{th} AIAA drag prediction workshop [49]. Simulations were carried out for $M_\infty = 0.85$, $C_L = 0.5$, and a reference wing Reynolds number of $Re_{C_{ref}} = 5 \times 10^6$. Analyses were conducted for the "clean-wing", as well as the "Through-Flow-Nacelle (TFN)" CRM configurations [38], to enable the evaluation of installation drag.

For the TFN CRM configuration mesh independence was evaluated using meshes consisting of 14×10^6, 30×10^6, and 50×10^6 elements. For the "clean-wing" CRM configuration, meshes with 7×10^6, 14×10^6, and 29×10^6 elements were used. For both configurations the GCI was below 1% with regards to the medium mesh. The airframe drag coefficient was determined within approximately 13 drag counts of the measured data. These results are in agreement with those reported in the literature [54].

The method was further validated by quantifying its ability to predict the installation drag $C_D^{Inst.}$ [53] (Fig. 7(a)). Within this work, $C_D^{Inst.}$ is defined as the difference in drag between the Wing-Body-Nacelle-Pylon (WBNP) and Wing-Body (WB) CRM configurations. Analyses were carried out using the medium grid for $C_L \in (\approx 0.2, \approx 0.6)$. The simulations were able to reproduce the experimental trends, and the difference in $C_D^{Inst.}$ between CFD model prediction and measured data was less than 8 drag counts across the C_L range. For the design CRM conditions of $M_\infty = 0.85$ and $C_L = 0.5$, the installation drag was over-predicted by approximately 2 drag counts.

The Dual Separate Flow Reference Nozzle (DSFRN) [55] was used as a CFD validation test case for exhaust performance. Anal-

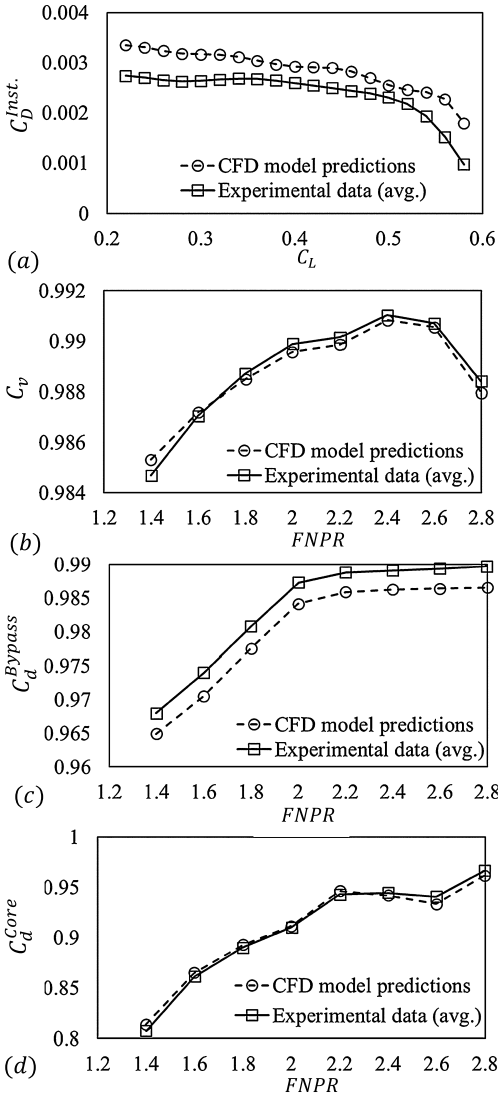

Fig. 7. Installed engine model validation - comparison with averaged experimental data [53,55]: (a) installation drag $C_D^{inst.}$, (b) exhaust velocity coefficient C_v, (c) bypass nozzle discharge coefficient C_d^{Bypass}, (d) core nozzle discharge coefficient C_d^{Core}.

yses were performed for a Fan Nozzle Pressure Ratio ($FNPR = \frac{P_0^{fan}}{p_\infty}$) range between 1.4 and 2.8 and for ground-level static conditions ($M_\infty \approx 0$) [55] (Figs. 7(b)-(c)). A fixed Extraction Ratio of ($ER = \frac{FNPR}{CNPR} = 1.2$) was applied, where CNPR is the Core Nozzle Pressure Ratio $CNPR = \frac{P_0^{core}}{p_\infty}$. A mesh independence analysis was carried out using meshes with 40×10^6, 80×10^6, and 120×10^6 elements for $FNPR = 2.2$. A difference in C_v of 0.003% was found between the medium and fine meshes. The Root Mean Square (RMS) distance between CFD predictions and the averaged measured data [55] across the $FNPR$ range ((Figs. 7(b)-(c))), was found to be of the order of 0.033%, 0.32%, and 0.44% for C_v, C_d^{Bypass}, and C_d^{Core}, respectively

3. Results and discussion

3.1. Aircraft architecture and propulsion system integration

The wing/body/horizontal-tail version of the NASA CRM geometry was used [38]. Aerodynamic analyses were conducted at DP

Table 1
Engine cycle characteristics and operating conditions.

Engine cycle characteristic	Value
Design point	mid-cruise
Bypass ratio (BPR)	15+
Nominal mid-cruise standard net thrust $F_N^{Nom.}$	$\approx$ 60 kN
$FNPR = \frac{P_0^3}{p_\infty}$	$\approx$ 2.2
$CNPR = \frac{P_0^5}{p_\infty}$	$\approx$ 1.5
$MFCR = \frac{A_0}{A_{hi}}$	$\approx$ 0.7
Operating conditions	
M_∞	0.85
Altitude	10668 m

mid-cruise conditions with $M_\infty = 0.85$, $Re_{C_{ref}} \approx 45 \times 10^6$, and $C_L^{A/C} = \frac{(NVF)_L}{0.5\rho_\infty V_\infty^2 A_{ref}} = 0.5$ (Eq. (10a)), where A_{ref} is the CRM reference area [38]. The power-plant was representative of future large turbofans with $BPR \approx 15+$ [3] and a nominal standard net thrust rating $F_N^{Nom.}$ of approximately 60 kN [36] (Table 1). The exhaust was optimised by Goulos et al. [4]. The engine had a three-dimensional (3D) nacelle optimised using the method developed by Tejero et al. [32,33]. The intake was also drooped and scarfed (Fig. 1(c)). The intake highlight plane area A_{hi} was sized for an intake Mass Flow Capture Ratio of $MFCR = \frac{A_0}{A_{hi}} \approx 0.7$ at mid-cruise conditions (Fig. 3(b)). The engine cycle was based on publicly available information for a "year 2025 to 2030" entry to service technology level [1]. The cycle parameters in terms of Overall Pressure Ratio (OPR), Turbine Entry Temperature (TET), and component polytropic efficiencies were selected according to this technology level [1]. The $FNPR$ and $CNPR$ values were derived on the basis of minimising SFC at mid-cruise conditions. The engine cycle derivation was documented by Goulos et al. [6,36].

Numerical analyses were carried out for a total of 12 podded under-wing installation positions (Fig. 8). Each position was defined in terms of axial and vertical offset of the nacelle top-line Trailing Edge (TE) point, relative to the local wing Leading Edge (LE) coordinates (Fig. 8(a)). The span-wise location of the engine was held constant and defined according to the CRM TFN top-line TE coordinates [38]. The engine pitch and toe angles were defined as per the CRM TFN configuration with $\theta_{pitch} = 1.75°$ and $\theta_{toe} = 2.25°$ (Fig. 4) [38]. The normalised axial offset from the wing LE to the nacelle TE $\left(\frac{dx}{C}\right)$ varied between -0.05 and 0.05 to encompass both contemporary as well as close coupled positions (Fig. 8(b)). The vertical offset relative to the wing LE $\left(\frac{dz}{C}\right)$ varied between 0.05 and 0.15, depending on axial offset. This was done to assess whether a larger vertical offset can mitigate the impact of adverse flow features that can appear at close coupled positions due to interaction effects [10,11].

3.2. Net vehicle force variation across installation position design space

Fig. 9 presents the variation of NVF (Eq. (11)), as well as its constituent elements in terms of $(NPF)_D^{Cycle}$ and $D_{A/F} = (\phi_{airframe})_D$ across the investigated range of installation positions. Results are presented as local percentage differences of the quantity of interest, normalised with the power-plant's nominal standard net thrust rating $F_N^{Nom.}$ as written below:

$$\Delta(NVF)(\%) = 100 \times \frac{(NVF)^{local} - (NVF)^{max}}{F_N^{Nom.}} \quad (12)$$

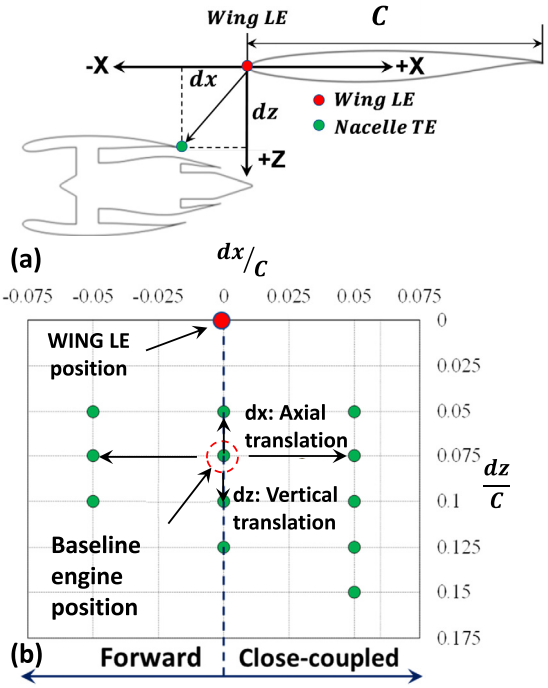

Fig. 8. Investigated engine installation positions: (a) notation and (b) investigated positions.

with similar expressions used for the variations of $\Delta(NPF_D^{Cycle})(\%)$ and $\Delta(D_{A/F})(\%)$ presented in Figs. 9(b) and (c), respectively.

Fig. 9(a) shows that the computed variation of $\Delta(NVF)(\%)$ across the range of installation positions (Fig. 8(b)) is of the order of 2.7%. It can be observed that the behaviour of NVF is governed both by axial (dx) as well as vertical (dz) gradients in terms of engine position. The maximum deficit of NVF is for the most close coupled position which is located at $\left(\frac{dx}{C}\right) = 0.05$ and $\left(\frac{dz}{C}\right) = 0.05$. This NVF penalty is mitigated with increasing axial as well as vertical offset, dx and dz, respectively. Furthermore, NVF is maximised for a "co-incident" engine location with a relatively large vertical offset, where the engine position corresponds to $\left(\frac{dx}{C}\right) = 0.0$ and $\left(\frac{dz}{C}\right) = 0.0125$.

This variation of NVF across the design space can be deciphered by decomposing it to its constituent elements, $(NPF)_D^{Cycle}$ and $D_{A/F}$ (Figs. 9(b) and (c)). Fig. 9(b) shows that the variation range for $\Delta(NPF_D^{Cycle})(\%)$ is roughly 11%. This is greater than the changes in $\Delta(NVF)(\%)$ (Fig. 9(a)) by more than a factor of 4, with the engine $(NPF)_D^{Cycle}$ reducing notably for close coupled positions. Furthermore, it can be noticed that the behaviour of $(NPF)_D^{Cycle}$ is primarily affected by the axial position of the engine $\left(\frac{dx}{C}\right)$, whilst vertical offset $\left(\frac{dz}{C}\right)$ exhibits a secondary role.

Fig. 9(c) shows that $D_{A/F}$ varies by about 13% of $F_N^{Nom.}$ across the range of positions. The relative magnitude of the effect of installation is similar to $(NPF)_D^{Cycle}$ (Fig. 9(b)). However, the trends for $(NPF)_D^{Cycle}$ and $D_{A/F}$ are in opposition (Fig. 9(b) and (c)). The associated variability in airframe trim incidence angle $\alpha_{A/F}$ was found to be negligible. Therefore, the changes noted for $D_{A/F}$ in Fig. 9(c) are primarily due to aerodynamic interaction effects, rather than due to the influence of aircraft re-trim. Overall, the coupled airframe-engine performance, as expressed by NVF, depends on the balance between $(NPF)_D^{Cycle}$ (Fig. 9(b)) and $D_{A/F}$

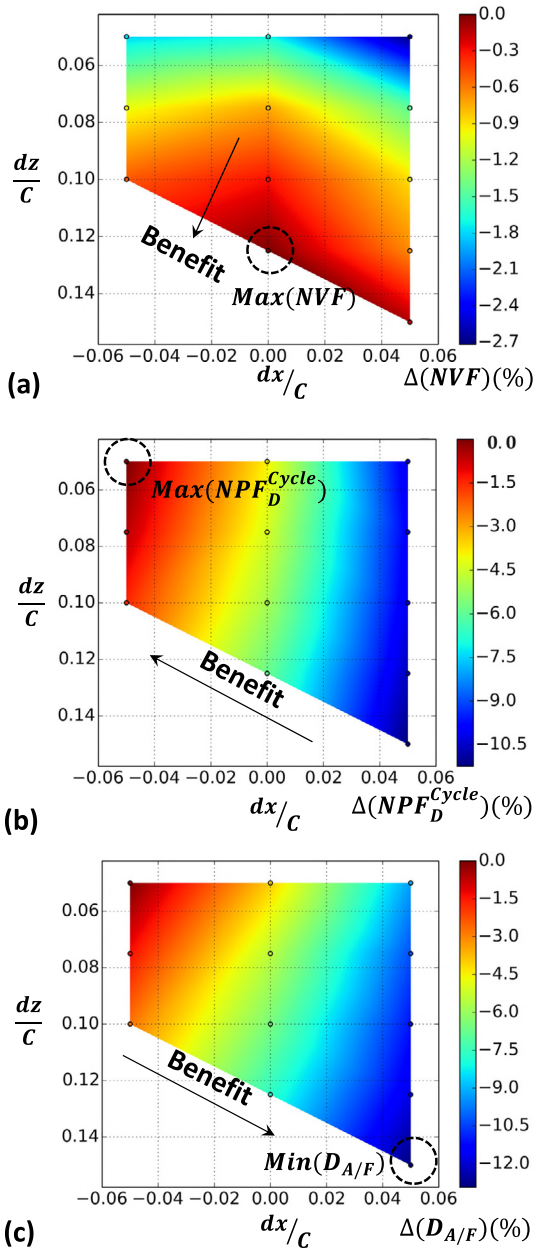

Fig. 9. Variation of coupled airframe-engine aerodynamic performance: (a) net vehicle force $\Delta(NVF)(\%)$, (b) net propulsive force $\Delta(NPF_D^{Cycle})(\%)$, and (c) airframe drag $\Delta(D_{A/F})(\%)$.

(Fig. 9(c)). Since $(NPF)_D^{Cycle}$ and $D_{A/F}$ exhibit conflicting gradients, the optimum NVF region is dictated by the most beneficial trade-off between engine ($(NPF)_D^{Cycle}$) and airframe ($D_{A/F}$) performance. This results in variations of NVF across the design space that are relatively small compared to the variability observed for $(NPF)_D^{Cycle}$ and $D_{A/F}$. This is due to the partial offset between engine and airframe installation effects.

3.3. Net propulsive force decomposition and synthesis of net vehicle force

The behaviour of $(NPF)_D^{Cycle}$ (Fig. 9(b)) was decomposed to its constituent elements of exhaust and nacelle aerodynamic performance. Figs. 10(a) and (b) present the impact of engine installation position on the modified exhaust gross propulsive force $(GPF^*)_D^{Cycle}$ and modified nacelle drag D_{nac}^*. Results are presented

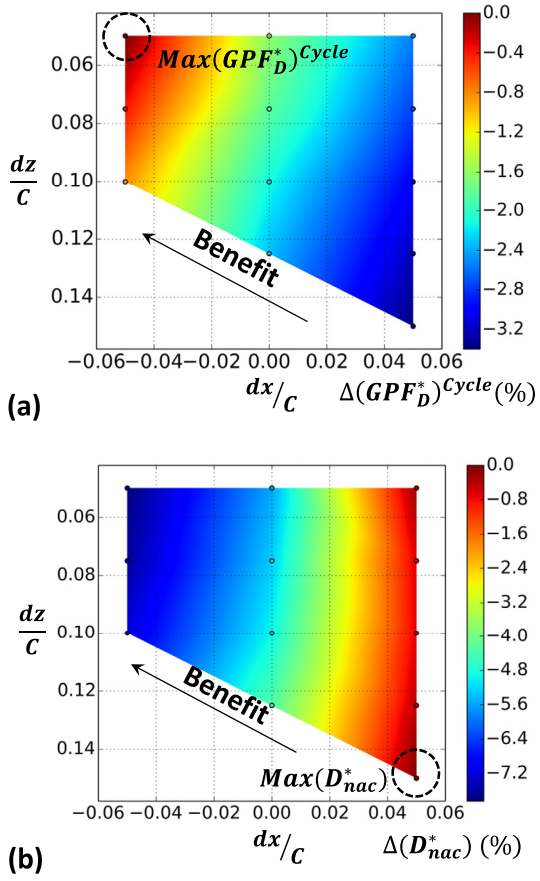

Fig. 10. Variation of normalised exhaust and nacelle performance: (a) modified gross propulsive force $\Delta(GPF_D^*)^{Cycle}(\%)$, and (b) modified nacelle drag $\Delta(D_{nac}^*)(\%)$.

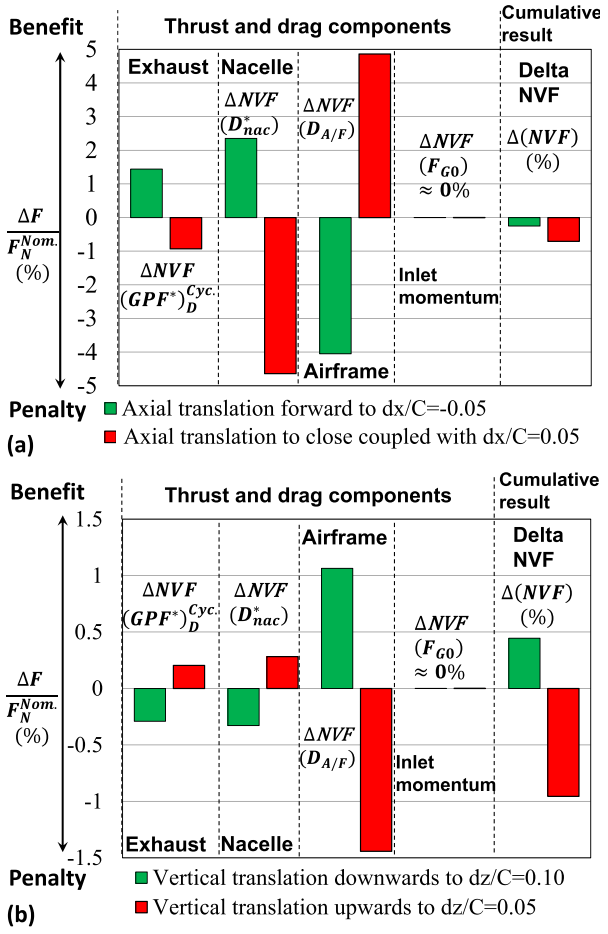

Fig. 11. Synthesis of $\Delta(NVF)(\%)$ due to changing engine installation position from baseline ($\left(\frac{dx}{C}\right) = 0.0$ and $\left(\frac{dz}{C}\right) = 0.075$) (Fig. 8(b)): (a) axial translation and (b) vertical translation.

as local percentage differences of $F_N^{Nom.}$ using a normalisation similar to that described by Eq. (12) and also applied in Fig. 9. This was done to express the impact of installation position on the two engine related terms using a common measurement unit. This enabled the identification of the dominant terms that influence the synthesis of $(NPF)_D^{Cycle}$ and NVF.

Both the exhaust and the nacelle exhibit a deficit in aerodynamic performance for close coupled engine positions, with $(GPF^*)_D^{Cycle}$ reducing and D_{nac}^* increasing relative to forward engine locations (Fig. 8). The aerodynamic performance of the exhaust (Fig. 10(a)) is affected by the impact of both axial dx as well as vertical engine position dz. The nacelle is primarily affected by the effect of axial engine offset relative to the wing LE (Fig. 10(b)).

$(GPF^*)_D^{Cycle}$ varies by about -3.2% which is primarily associated with the effect of engine installation on the modified exhaust velocity coefficient $(C_v^*)_D$. This effect was omitted in previous TDB approaches developed for the prediction of installed engine performance [22]. However, the TDB system developed in this work takes into account this effect in the formulation of $(NPF)_D^{Cycle}$ (Eq. (9)) and ultimately NVF (Eq. (11)). The variation of D_{nac}^* across the range of installation positions is greater than the changes in $(GPF^*)_D^{Cycle}$ by a factor of approximately 2.4. This indicates that the installed engine net propulsive force $(NPF)_D^{Cycle}$ (Fig. 9(b)), is primarily affected by the impact of installation position on modified nacelle drag D_{nac}^* (Fig. 10(a)), and secondarily on the exhaust $(GPF^*)_D^{Cycle}$ (Fig. 10(b)).

Fig. 11 illustrates the synthesis of $\Delta(NVF)(\%)$ associated with axial and vertical engine translation relative to a nominal position of $\left(\frac{dx}{C}\right) = 0.0$ and $\left(\frac{dz}{C}\right) = 0.075$ (Fig. 8(b)). To highlight the influence of the constituent thrust and drag components, $\Delta(NVF)(\%)$ is decomposed to the effect of installation position on the exhaust $\Delta NVF(GPF^*)_D^{Cycle}$, the nacelle $\Delta NVF(D_{nac}^*)$, and the airframe $\Delta NVF(D_{A/F})$. Results are presented as percentage differences of the quantity of interest, normalised with $F_N^{Nom.}$ as written below:

$$\Delta(NVF)(\%) = 100 \times \frac{(NVF)^{Translated} - (NVF)^{Baseline}}{F_N^{Nom.}} \tag{13}$$

with similar expressions used for the impact of the exhaust $\Delta NVF(GPF^*)_D^{Cycle}$, the nacelle $\Delta NVF(D_{nac}^*)$, and the airframe $\Delta NVF(D_{A/F})$.

Fig. 11(a) shows that there is a penalty in NVF associated with translating the engine axially, relative to the baseline position. The associated values of $\Delta(NVF)(\%)$ are -0.25% and -0.70% for translating the engine to a forward ($\left(\frac{dx}{C}\right) = -0.05$) and to a close coupled position ($\left(\frac{dx}{C}\right) = 0.05$), respectively. These values of $\Delta(NVF)(\%)$ are the cumulative results of notably larger thrust and drag component changes due to the effect of installation on exhaust, nacelle, and airframe aerodynamics. These differences in the constituent thrust and drag components can be conflicting, and can be up to an order of magnitude higher compared to $\Delta(NVF)(\%)$. Furthermore, although both the close coupled and forward positions have a penalty in NVF, the breakdown of the

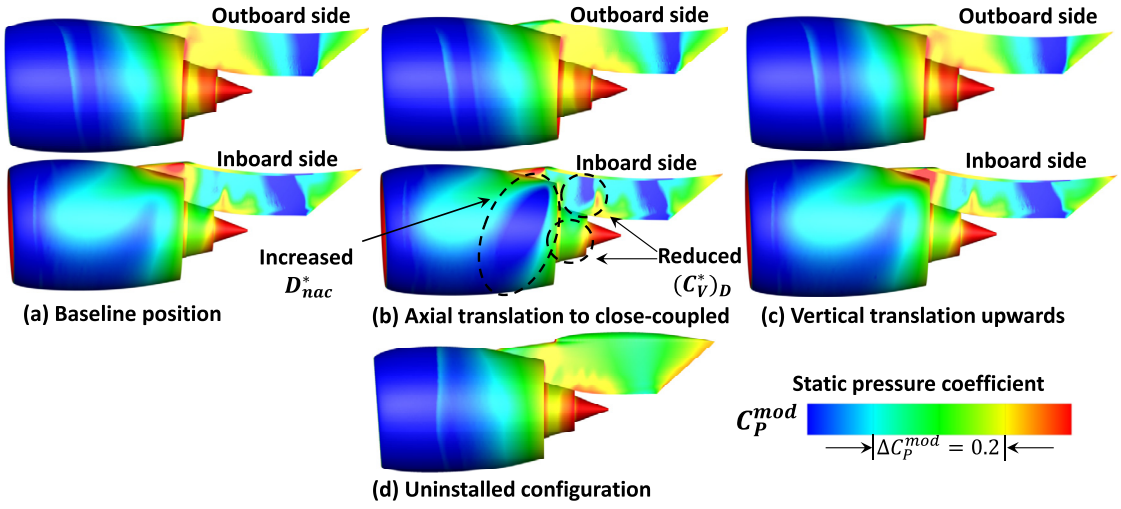

Fig. 12. Normalised static pressure distribution on aero-engine surfaces for investigated installation positions: (a) baseline ($\left(\frac{dx}{C}\right) = 0.0$ and $\left(\frac{dz}{C}\right) = 0.075$), (b) axial translation to close coupled ($\left(\frac{dx}{C}\right) = 0.05$ and $\left(\frac{dz}{C}\right) = 0.075$), (c) vertical translation upwards ($\left(\frac{dx}{C}\right) = 0.0$ and $\left(\frac{dz}{C}\right) = 0.05$), and (d) uninstalled engine configuration.

constituent thrust and drag components differs significantly between each case. In both cases, $\Delta(NVF)(\%)$ is governed predominantly by the impact of installation position on the nacelle and the airframe. The associated ranges of variation are $\Delta NVF(D^*_{nac}) \approx 7\%$ and $\Delta NVF(D_{A/F}) \approx 9\%$, respectively, across the two positions. A smaller variability of $\Delta(NVF)(\%)$ is observed due the impact of axial engine translation on the exhaust, with $\Delta NVF(GPF^*)_D^{Cycle} \approx 2.4\%$ across the two positions. This change in exhaust aerodynamic behaviour due to the impact of installation has not been previously accounted for in established near-field TDB methods [22,23]. However, these differences in exhaust performance are significant compared to the overall values of $\Delta(NVF)(\%)$ (Fig. 11(a)), and cannot be neglected in the analysis of coupled engine-airframe architectures.

Fig. 11(b) presents the impact of vertical engine translation on the synthesis of NVF. It is noted that the numerical synthesis of NVF is described by Eqs. (9) and (11). The corresponding values of $\Delta(NVF)(\%)$ are +0.45% and -0.95% for moving the engine to a downward ($\left(\frac{dz}{C}\right) = 0.10$) and to an upward position ($\left(\frac{dz}{C}\right) = 0.05$), respectively. It is noted that vertical engine translation distance is reduced by a factor of two (2) relative to the case of axial movement (Fig. 8(b)). However, the magnitude of the changes noted in the thrust and drag components is reduced by a factor of four (4) (Fig. 11(a)). This indicates that the aerodynamic sensitivities across the range of installation positions are governed primarily by the impact of axial engine position.

For the case of vertical engine movement, the impact of installation position on the airframe is the dominant parameter (Fig. 11(b)). This variation in airframe drag is approximately $\Delta NVF(D_{A/F}) \approx 2.5\%$ across the two engine positions (Fig. 11(b)). Similarly to the case of axial engine translation (Fig. 11(a)), the polarity in the changes noted for the thrust and drag components is reversed with the gradient of translation. However, the differences noted in the performance of the nacelle and the exhaust are of similar magnitude, with $\Delta NVF(D^*_{nac}) \approx 0.6\%$ and $\Delta NVF(GPF^*)_D^{Cycle} \approx 0.5\%$, respectively.

Therefore, the impact of engine installation on overall aircraft performance depends on the balance between significant and conflicting aerodynamic effects on the airframe, the nacelle, and the exhaust. The approach described in this paper expresses this balance using the concept of NVF. The proposed method introduces the impact of engine installation on exhaust performance which was omitted in previous TDB methods [22]. This effect was shown to account for nearly 25% of the changes noted in $\Delta(NPF)_D^{Cycle}$ across the range of engine positions (Fig. 10). These changes were shown to be of the same order of magnitude as the differences in NVF (Fig. 9(a)). Hence, it is essential to include the impact of installation on the exhaust for the correct determination of overall airframe-engine performance for close coupled architectures.

3.4. Impact of installation position on aero-engine aerodynamic behaviour

Fig. 12 presents the aerodynamic behaviour of the nacelle, exhaust, and pylon for the baseline and close coupled installation positions assessed in Fig. 11. Results are presented in terms of normalised static pressure distribution $C_p^{mod} = \frac{p - p_\infty}{p_\infty}$ on the aero-engine outboard and inboard surfaces (Fig. 2). Predictions are presented for the baseline, axially close coupled, and vertically close coupled positions in Figs. 12(a), (b), and (c), respectively. To highlight the impact of installation on the engine aerodynamic behaviour, predictions were also carried out for an uninstalled engine at identical operating conditions without the presence of the airframe (Fig. 12(d)).

Figs. 12(a), (b), and (c) reveal notable differences between the installed engine outboard and inboard side transonic flow topologies, for all three (3) installation positions, relative to the uninstalled engine (Fig. 12(d)). These flow differences are primarily due to the impact of the "aerodynamic channel" that is formed between the fuselage, wing, and the engine inboard side (Fig. 2). This leads to increased flow acceleration due to the effective flow area restriction, which results in reduced static pressure C_p^{mod} on the nacelle, exhaust after-body, and pylon inboard side, when compared to the outboard flow topology. Furthermore, due to the wing sweep angle, the inboard side of the aero-engine geometry is axially more overlapped with the wing compared to the outboard side (Fig. 2), resulting in increased aerodynamic interaction effects [15]. Thus, the identified aerodynamic channel effect, in combination with the geometric characteristics of a swept transonic wing, result in notable flow asymmetry between the engine outboard and inboard sides (Fig. 12).

Figs. 12(a), (b), and (c) show that the impact of close coupling the engine with the airframe has a relatively small effect on the transonic flow topology on the engine outboard side, compared to the uninstalled engine (Fig. 12(d)). The aerodynamic behaviour on the outboard side appears to remain unaffected when the engine is moved from the baseline (Fig. 12(a)) to the axially close coupled position (Fig. 12(b)). The inboard flow topology is influenced significantly by the impact of airframe-engine integration. Specifically, an increasingly large region of reduced static pressure C_p^{mod} can be observed on the inboard side of the nacelle after-body for the axially close coupled position (Fig. 12(b)) relative to the baseline location (Fig. 12(a)). This is due to the amplification of the aerodynamic channel effect (Fig. 2). This is also the primary flow mechanism responsible for the increase noted in D_{nac}^{*} (Fig. 11(a)), which reaches roughly 4.6% of $F_N^{Nom.}$, due to the impact of close coupled airframe-engine interaction.

Furthermore, Fig. 12(b) reveals the formation of strong normal shock on the inboard side of the pylon for the axially close coupled engine position, at the axial location of the core after-body TE. This manifests within both thrust and drag domains of the pylon (Fig. 3(b)) and is notably weaker for the baseline position (Fig. 12(a)). This arises due to the close proximity of the nacelle flow and exhaust stream-tube boundary to the wing. This leads to the formation of an effective "gully flow" between the core after-body and the wing, resulting in a local flow over-acceleration that terminates with a shock. Overall, these effects result in reduced static pressure on the core after-body for the close coupled position (Fig. 12(b)), relative to the baseline location (Fig. 12(a)). These lead to a reduction of installed $(GPF^{*})_D^{Cycle}$ of 0.93% of F_N^{Nom} (Fig. 11(a)).

The combined effect of installation position on $(GPF^{*})_D^{Cycle}$ and D_{nac}^{*} results in a notable net propulsive force change of the order of $\Delta(NPF)_D^{Cycle} \approx -5.6\%$ of $F_N^{Nom.}$. However, this penalty in $(NPF)_D^{Cycle}$ is partially offset by a beneficial reduction in $D_{A/F}$ of 4.9% of $F_N^{Nom.}$ (Fig. 11(a)). It is interesting to note that the impact of the closer vertical position (Fig. 12(c)) has a negligible influence on the engine inboard side aerodynamic behaviour, relative to the baseline location (Fig. 12(a)). This indicates that the small changes noted in $(GPF^{*})_D^{Cycle}$ and D_{nac}^{*} within Fig. 11(b), are predominantly due to the changes noted on the engine outboard side flow topology.

3.5. Impact of installation position on exhaust discharge coefficients

The impact of engine installation position on the exhaust system discharge coefficients was quantified. C_d^{Bypass} varied by approximately 0.15% across the range of installation positions. This is because the bypass nozzle is choked with $FNPR \approx 2.2$, which renders its mean flow relatively insensitive to external pressure field variations. In contrast, the core nozzle is unchoked with $CNPR \approx 1.5$, which renders its mass flow and discharge coefficient more susceptible to the impact of the installed pressure field [21,15].

The variation range predicted for C_d^{Core} across the design space is of the order 5% (Fig. 13). The behaviour of C_d^{Core} is influenced by the "channel" and "gully flow" effects (Figs. 12(a), (b), and (c)), as well as by the transonic flow topology on the core after-body due to the choked bypass nozzle (Fig. 12(d)) [21]. The combined effect of these installation features results in reduced static pressure on the inboard side of the core after-body TE for close coupled positions (Fig. 12(b)) which lowers the base pressure at the core nozzle exit. Thus, the impact of external flow suppression due to the free-stream and bypass nozzle flows diminishes relative to forward positions and, as a result, C_d^{Core} increases.

As an example, it is noted that a change in the engine installation position from the baseline location (Fig. 12(a)) to the axially close coupled case (Fig. 12(b)) results in a C_d^{Core} increase of approximately 1.3%. From an exhaust design perspective, this may require a re-sizing the core nozzle throat to achieve the desired flow capacity and ensure that the power-plant operates near DP conditions. Fig. 13 shows that relatively small adjustments of core nozzle throat area are required for the engine positions of interest (Fig. 12)($\approx 1.3\%$) to mitigate the impact of the installed flow-field. As a result, it is unlikely that the process of core nozzle re-sizing would affect the modified exhaust velocity coefficient $(C_v^{*})_D$ which influences the computation of $(GPF^{*})_D^{Cycle}$ and consequently, NVF. Thus, these results support one of the key assumptions of this proposed TDB approach, which dictates that the performance of the exhaust will not be significantly affected by nozzle re-sizing requirements.

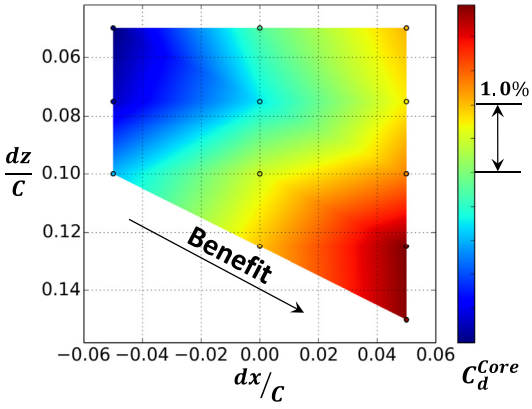

Fig. 13. Impact of engine installation position on core nozzle discharge coefficient C_d^{Core}.

4. Conclusions

This article described a novel thrust and drag accounting formulation for the aerodynamic assessment of integrated airframe-engine systems. An integral metric was proposed based on the concept of "net vehicle force", which quantifies the overall performance of coupled airframe-engine configurations. This was accomplished through the unification of near-field airframe, nacelle, and exhaust aerodynamic coefficients obtained from numerical flow solutions, combined with the engine cycle parameters derived from a thermodynamic model. The developed TDB methodology accounts for the impact of installation on the exhaust, and ensures compatibility between jet momentum and enthalpy efflux with the prescribed engine cycle characteristics. These aspects were ignored in previous TDB formulations. Therefore, the proposed method constitutes an enabling technology for the aerodynamic design and analysis of installed aero-engines.

It was shown using this method that installation effects due to the impact of a close coupled engine position can result in a net vehicle force difference of nearly −0.70% of nominal standard net trust, relative to a baseline location. It was demonstrated that this impact of installation position on overall aircraft performance depends on the balance between significant and conflicting aerodynamic effects on the airframe and the power-plant. Specifically, the associated differences observed in net propulsive force and airframe drag were of the order −5.6% and −4.9% of nominal standard net thrust, respectively. Furthermore, it was shown that C_d^{Core} may increase by 1.3% for translating the engine from a baseline location to a representative close coupled position, whilst C_d^{Bypass} was found to be practically insensitive due to choked flow conditions.

5. Data statement

Due to commercial confidentiality agreements the supporting data is not available.

Declaration of competing interest

The authors declare that they have no known competing financial interests or personal relationships that could have appeared to influence the work reported in this paper.

Acknowledgements

This project was funded by Innovate UK (TSB 113075).

References

[1] F. Haselback, A. Newby, R. Parker, Next generation of large civil aircraft engines - concepts & technologies, in: European Turbomachinery Conference, Madrid, Spain, 23–27 March 2015.
[2] N.T. Birch, 2020 vision: the prospects for large civil aircraft propulsion, Aeronaut. J. 104 (1038) (August 2000) 347–352.
[3] A.H. Epstein, Aeropropulsion for commercial aviation in the twenty-first century and research directions needed, AIAA J. 52 (5) (May 2014) 901–911.
[4] I. Goulos, J. Otter, T. Stankowski, D. MacManus, N. Grech, C. Sheaf, Design optimisation of separate-jet exhausts for the next generation of civil aero-engines, Aeronaut. J. 122 (1256) (October 2018).
[5] D. Dusa, D. Lahti, D. Berry, Investigation of Subsonic Nacelle Performance Improvement Concept, 18th Joint Propulsion Conference, No. A82-37676, Cleveland, OH, U.S.A., June 21-23 1982.
[6] I. Goulos, T. Stankowski, D. MacManus, P. Woodrow, C. Sheaf, Civil turbofan engine exhaust aerodynamics: impact of bypass nozzle after-body design, Aerosp. Sci. Technol. 73 (2) (February 2018) 85–95.
[7] M. Waters, E. Schairer, Analysis of Turbofan Propulsion System Weight and Dimensions, NASA, TM X-73, Ames Research Center, Moffet Field, California, January 1977.
[8] D.L. Daggett, Ultra Efficient Engine Technology Systems Integration and Environmental Assessment, NASA, NASA/CR-2002-21175, Boeing Commercial Airplane Group, Seattle, Washington, 2002.
[9] D.L. Berry, The Boeing 777 Engine/Aircraft Integration Aerodynamic Design Process, ICAS Congress 1994, No. ICAS-94-6.4.4, Anaheim, CA, 1994, pp. 1305–1320.
[10] H.F.V. Geyr, C.C. Rosscow, A Correct Thrust Determination Method for Turbine Powered Simulations in Wind Tunnel Testing, 41st AIAA/ASME/SAE/ASEE Joint Propulsion Conference & Exhibit, No. AIAA 2005-3707, July 2005.
[11] L. Wiart, O. Atinault, B. Paluch, D. Hue, R. Grenon, Development of NOVA Aircraft Configurations for Large Engine Integration Studies, 33rd AIAA Applied Aerodynamics Conference, No. AIAA 2015-2254, June 2015.
[12] T. Stankowski, D. MacManus, M. Robinson, C. Sheaf, Aerodynamic effects of propulsion integration for high bypass ratio engines, J. Aircr. 54 (6) (November-December 2017) 2270–2284.
[13] T. Sibili, M. Savil, V. Sethi, D. MacManus, A. Rolt, Numerical Simulation of Propulsion Systems Integration for Very High Bypass Ratio Engines, Proceedings of ASME Turbo Expo - Turbine Technical Conference and Exposition, No. GT2012-68908, Copenhagen, Denmark, June 2012.
[14] D.L. Daggett, S. Brown, R.T. Kawai, Ultra Efficient Engine Diameter Study, NASA, CR-2003-212309, Boeing Commercial Airplane Group, Seattle, Washington, 2003.
[15] J. Otter, T. Stankowski, M. Robinson, D. MacManus, Installation aerodynamics of civil aero-engine exhaust systems, Aerosp. Sci. Technol. 89 (2019) (June 2019).
[16] E.E. Covert, C.R. James, W.M. Kimsey, G.K. Rickey, E. Rooney, Thrust and Drag: Its Prediction and Verification, Progress in Astronautics and Aeronautics Series, American Institute of Aeronautics & Astronautics, Reston, VA, 1985.
[17] Advanced Ducted Propulsor In-Flight Thrust Determination, SAE International, Aerospace Information Report, AIR5450, 2008.
[18] Guide to In-Flight Thrust Measurement of Turbojets and Fan Engines, MIDAP Study Group, Advisory Group for Aerospace Research and Development, AGARDograph No. 237, 7 Rue Ancelle 92200 Newilly, Sur Seine, France, January 1979.
[19] M. Bauer, J. Friedrichs, D. Wulff, C. Werner-Spatz, Development and Validation of an On-Wing Engine Thrust Measurement System, ASME Turbo Expo 2017: Turbomachinery Technical Conference and Exposition, No. GT2017-63277, Charlotte, NC USA, 2017.
[20] ESDU, The Determination of Gross Thrust and Mass flow in Flight. (Air Breathing Ducted-Flow Engines with Convergent Nozzles), ESDU 69007, 1981.
[21] J. Otter, I. Goulos, D. MacManus, M. Slaby, Aerodynamic analysis of civil aero-engine exhaust systems using computational fluid dynamics, J. Propuls. Power 34 (5) (September-October 2018) 1152–1165.
[22] Z. Yufei, C. Haixin, F. Song, Z. Miao, Z. Meihong, Drag prediction method of powered-on civil aircraft based on Thrust-Drag bookkeeping, Chin. J. Aeronaut. 28 (4) (August 2015) 1023–1033.
[23] L. Jing, G. Zhenghong, H. Jiangtao, Z. Ke, Aerodynamic design optimization of nacelle/pylon position on an aircraft, Chin. J. Aeronaut. 26 (4) (August 2013) 850–885.
[24] D. Destarac, J.V. der Vooren, Drag/thrust analysis of jet-propelled transonic transport aircraft; definition of physical drag components, Aerosp. Sci. Technol. 8 (6) (September 2004) 545–556.
[25] B. Malouin, J.-Y. Trepanier, E. Laurendeau, Installation and interference drag decomposition via RANS far-field methods, Aerosp. Sci. Technol. 54 (7) (July 2016) 132–142.
[26] J.B. Vos, S. Sanchi, A. Gehri, Drag prediction workshop 4 results using different grids including near-field/far-field drag analysis, J. Aircr. 50 (5) (September-October 2013) 1615–1627.
[27] M. Gariepy, B. Malouin, J.-Y. Trepanier, E. Laurendeau, Far-field drag decomposition applied to the drag prediction workshop 5 cases, J. Aircr. 50 (6) (November-December 2013) 1822–1831.
[28] T. Zhaoguang, C. Yingchun, S. Jiangtao, Study of power influences to the wing-mounted civil aircraft aerodynamic characteristics, J. Aircr. 51 (2) (March-April 2014) 629–636.
[29] W. Zheng, Y. Wang, J. Shan, X. Deng, W. Tian, Interference mechanism of engine exhaust on civil aircraft drag performance, J. Aircr. 49 (6) (November-December 2012) 2001–2006.
[30] T. Stankowski, D.G. MacManus, C. Sheaf, R. Christie, Aerodynamics of aero-engine installation, Proc. Inst. Mech. Eng., G J. Aerosp. Eng. 230 (14) (February 2016) 2673–2692.
[31] F. Zhu, N. Qin, Intuitive class/shape function parameterization for airfoils, AIAA J. 52 (1) (January 2014) 17–25.
[32] F. Tejero, M. Robinson, D. MacManus, C. Sheaf, Multi-objective optimisation of short nacelles for high bypass ratio engines, Aerosp. Sci. Technol. 91 (August 2019) 410–421.
[33] F. Tejero, D. MacManus, C. Sheaf, Surrogate-based aerodynamic optimisation of compact nacelle aero-engines, Aerosp. Sci. Technol. 93 (2019) (October 2019).
[34] R. Christie, A. Heidebrecht, D. MacManus, An automated approach to nacelle parameterization using intuitive class shape transformation curves, J. Eng. Gas Turbines Power 139 (6) (June 2017) 062601.
[35] R. Christie, M. Robinson, F. Tejero, D. MacManus, The use of hybrid intuitive class shape transformation curves in aerodynamic design, Aerosp. Sci. Technol. 95 (December 2019) 105473.
[36] I. Goulos, T. Stankowski, J. Otter, D. MacManus, N. Grech, C. Sheaf, Aerodynamic design of separate-jet exhausts for future civil aero-engine, part 1: parametric geometry definition and CFD approach, J. Eng. Gas Turbines Power 138 (8) (August 2016) 081201.
[37] I. Goulos, J. Otter, T. Stankowski, D. MacManus, N. Grech, C. Sheaf, Aerodynamic design of separate-jet exhausts for future civil aero-engines, part 2: surrogate modeling and optimization, J. Eng. Gas Turbines Power 138 (8) (August 2016) 081202.
[38] J.C. Vassberg, M.A. Dehaan, M.B. Rivers, R.A. Wahls, Development of a Common Research Model for Applied CFD Validation Studies, 26th AIAA Applied Aerodynamics Conference, No. AIAA Paper 2008-6919, 2008.
[39] P. Walsh, P. Fletcher, Gas Turbine Performance, Blackwell Publishing, 2004.
[40] J. Otter, Aerodynamics and Performance of Civil Aero-Engine Exhaust Systems, PhD Thesis, Cranfield University, Cranfield, Bedfordshire, MK430AL, 2018.
[41] Ansys Inc., 275 Technology Drive, Canonsburg, PA 15317, ANSYS WORKBENCH User's Guide.
[42] ANSYS, I., ANSYS FLUENT Theory Guide: Release 16.2, ANSYS, Canonsburg, PA, 2013, 2013.
[43] I. Goulos, D. MacManus, C. Sheaf, Civil turbofan engine exhaust aerodynamics: impact of fan exit flow characteristics, Aerosp. Sci. Technol. 93 (2019) 105181.
[44] W.L. Macmillan, Development of a Module Type Computer Program for the Calculation of Gas Turbine Off Design Performance, Ph.D. thesis, Department of Power and Propulsion, Cranfield University, 1974.
[45] V. Pachidis, P. Pilidis, L. Marinai, I. Templalexis, Towards a full two dimensional gas turbine performance simulator, Aeronaut. J. 111 (1121) (2007) 433–442.
[46] Y.G. Li, L. Marinai, E.L. Gatto, V. Pachidis, P. Pilidis, Multiple-point adaptive performance simulation tuned to aeroengine test-bed data, J. Propuls. Power 25 (3) (2009) 635–641.
[47] I. Uyioghosa, M. Goiricelaya, D. Nalianda, O. Minervino, Aero engine compressor fouling effects for short- and long-haul missions, Proc. Inst. Mech. Eng., G J. Aerosp. Eng. 230 (7) (October 2016) 1312–1324.
[48] R. Christie, S. Ramirez, D. MacManus, Aero-engine installation modelling and the impact on overall flight performance, in: Advanced Aero Concepts, Design and Operations Conference, vol. 27, Royal Aeronautical Society (RAeS), 2014.
[49] J.C. Vassberg, E.N. Tinoco, M. Mani, B. Rider, Summary of the fourth AIAA CFD drag prediction workshop, in: 29th AIAA Applied Aerodynamics Conference, 2010.
[50] I.B. Celik, U. Ghia, P.J. Roache, C.J. Freitas, H. Coleman, P.E. Raad, Procedure for estimation and reporting of uncertainty due to discretization in CFD applications, J. Fluids Eng. 130 (July 2008).

[51] D.C. Wilcox, Comparison of two-equation turbulence models for boundary layers with pressure gradient, AIAA J. 31 (8) (August 1993) 1414–1421.
[52] W. Sutherland, The viscosity of gases and molecular forces, Philos. Mag. 36 (1893) 507–531.
[53] M. Rivers, A. Dittberner, Experimental Investigations of the NASA Common Research Model in the NASA Langley National Transonic Facility and NASA Ames 11-Ft Transonic Wind Tunnel (Invited), 49th AIAA Aerospace Sciences Meeting including the New Horizons Forum and Aerospace Exposition, No. AIAA 2011-1126, Orlando, Florida, 6 2011.
[54] D. Levy, K.R. Laflin, E.N. Tinoco, J.C. Vassberg, M. Mani, B. Rider, C. Rumsey, H. Joseph, R.A.W. Morisson, O.P. Brodersen, S. Crippa, D. Mavriplis, M. Murayama, Summary of Data from the Fifth AIAA CFD Drag Prediction Workshop, 51st AIAA Aerospace Sciences Meeting Including the New Horizons Forum and Aerospace Exposition, No. AIAA 2013-0046, 2013.
[55] K.L. Mikkelsen, D.J. Myren, D.G. Dahl, M.D. Christiansen, Initial Subscale Performance Measurements of the AIAA Dual Separate Flow Reference (DSFR) Nozzle, 51st AIAA/SAE/ASEE Joint Propulsion Conference, No. AIAA 2015-3883, Orlando, Florida, USA, 2015.